Predicting functional connectivity from structural connectivity via computational models using MRI: An extensive comparison study

Arnaud Messé [a,b,*], David Rudrauf [c,d], Alain Giron [b], Guillaume Marrelec [b]

[a] Department of Computational Neuroscience, University Medical Center Eppendorf, Hamburg University, Hamburg, Germany
[b] Laboratoire d'Imagerie Biomédicale, Sorbonne Universités, UPMC Univ Paris 06, Inserm, CNRS, UMCR 2, UMRS 1146, UMR 7371, Paris, France
[c] Fonctions Cérébrales et Neuromodulation, Université Joseph Fourier, Grenoble, France
[d] Inserm, U836, Grenoble Institut des Neurosciences, Grenoble, France

ARTICLE INFO

ABSTRACT

The relationship between structural connectivity (SC) and functional connectivity (FC) in the human brain can be studied using magnetic resonance imaging (MRI). However many of the underlying physiological mechanisms and parameters cannot be directly observed with MRI. This limitation has motivated the recent use of various computational models meant to bridge the gap. However their absolute and relative explanatory power and the properties that actually drive that power remain insufficiently characterized. We performed an extensive comparison of seven mainstream computational models predicting FC from SC. We investigated the extent to which simulated FC could predict empirical FC. We also applied graph theory to the entire set of simulated and empirical FCs in order to further characterize the relationships between the models and the MRI data. The comparison was performed at three different spatial scales. We found that (i) there were significant effects of scale and model on predictive power; (ii) among all models, the simplest model, the simultaneous autoregressive (SAR) model, was found to consistently perform better than the other models; (iii) the SAR also appeared more 'central' from a graph theory perspective; and (iv) empirical FC only appeared weakly correlated with simulated FCs, and was featured as 'peripheral' in the graph analysis. We conclude that the substantial differences existing between these computational models have little impact on their predictive power for FC and that their capacity to predict FC from SC appears to be both moderate and essentially underlined by a simple core linear process embodied by the SAR model.

© 2015 Elsevier Inc. All rights reserved.

Introduction

Magnetic resonance imaging (MRI) has proven to be a valuable technique for studying non-invasively the architectures of structural connections and of functional interactions between anatomical regions in the brain. Structural connectivity (SC) can be estimated using diffusion-weighted imaging (DWI) based tractography, while direct and indirect functional interactions can be inferred based on resting-state functional MRI (rs-fMRI) using measures of functional connectivity (FC). Both measures of connectivity can be related in order to better understand the relationships between SC and FC at various scales, including how SC conditions and constrains FC. Beyond the analysis of empirical correlations between SC and FC, computational models of neuronal and hemodynamics have been used in an attempt to further bridge the explanatory gap between observed SC and FC (Horwitz, 1990; Breakspear et al., 2010; Woolrich and Stephan, 2013).

In the present study, we report on an extensive comparison of the performance of seven mainstream computational models that have been previously used for predicting FC from SC (Deco et al., 2008; Honey et al., 2009; Cabral et al., 2011, 2012; Deco and Jirsa, 2012; Messé et al., 2014). First, building upon previous reports (see, Messé et al., 2014, 2015), we investigated the extent to which simulated FCs could predict empirical FC using measures of predictive power, i.e. the correlation between simulated and empirical FC. Second, we applied graph theory to the simulated and empirical FCs in order to further characterize their relationships. The comparison was performed at three different spatial scales (based on parcellations that partitioned gray matter into 160, 461 and 825 regions). We observed that (i) there were significant effects of scale and model on predictive power; (ii) among all models, the simplest model, the simultaneous autoregressive (SAR) model, was found to consistently perform better than the other models; (iii) this model also appeared more 'central' from a graph theory perspective; and (iv) empirical FC only appeared weakly correlated with simulated FC, and was characterized as 'peripheral' in the graph analysis.

We conclude that these computational models, which display oscillatory behaviors and dynamics that can be quite different, mostly

* Corresponding author at: Department of Computational Neuroscience, University Medical Center Eppendorf, Hamburg University, Hamburg, Germany.
E-mail address: a.messe@uke.de (A. Messé).

differ in aspects that have little impact on their predictive power for FC over the range of parameters explored. As reflected in our graph analysis, beyond their differences, their ability to predict FC from SC appears to mostly reduce to that of a simple core linear process embodied by the SAR model.

Material and methods

The processing pipeline is summarized in Fig. 1.

Real data

Acquisition

Twenty one right-handed healthy volunteers were recruited within local community (11 males, mean age 22 ± 2.4 years). All participants gave written informed consent and the protocol was approved by the local ethics committee. Data were acquired using a 3T Siemens Trio TIM MRI scanner (CENIR, Paris, France). Resting-state fMRI series were recorded using a single-shot, gradient-recalled echo-planar imaging sequence (repetition time TR: 3290 ms; echo time TE: 31 ms; $1.5 \times 1.5 \times 2.5$ mm^3 voxels; 46 contiguous slices). Two hundred fMRI volumes were acquired, during 11 min. The subjects were instructed to remain eyes closed and to reduce any mental effort. DWI data were recorded using a single-shot, echo planar imaging sequence (TR: 13 s; TE: 121 ms; 2 mm^3 isotropic voxels; 68 contiguous slices). Fifty encoding directions with $b = 1000$ s/mm^2 and a non-weighted image were acquired for each subject. A three dimensional, T_1-weighted, magnetization prepared rapid gradient-echo volume was also acquired during the same scanning session (TR: 2.3 ms; TE: 2.98 ms; 1.1 mm^3 isotropic voxels). fMRI data were preprocessed using SPM5 software.[1] For each subject, the first 4 fMRI volumes were discarded to allow for T_1 equilibration, and the remaining 196 fMRI volumes were corrected for slice-timing and head motion, excessive motion (greater than 3 mm or 3°) was not present in any of the subjects' scans. The resulting data were then spatially smoothed using an isotropic 6 mm full-width-at-half-maximum Gaussian kernel. DWI images were corrected for eddy-current distorsions using FSL, release 4.1[2] (Smith et al., 2004). Spatial normalization using linear transformations (combination of 3 translations, 3 rotations and 1 scale factor), between fMRI and DWI data and the anatomical volume, were computed for each subjects using FSL. Non-linear spatial normalization was also computed from the T_1-weighted anatomical volume of each subject to the standard space of the Montreal Neurological Institute (MNI) for visualization purpose.

Regions of interest

The T_1-weighted anatomical volume of each subject was parcellated using Freesurfer [3] (Fischl et al., 2004) and the procedure described in Hagmann et al. (2008). The procedure segmented the brain into gray matter and white matter compartments, and distinguished cortical and sub-cortical structures. A labeled cortical surface from an average template brain was registered onto the individual cortical surfaces, yielding a partition of the cerebral cortex of each subject into 160 regions (80 per hemisphere). Next, the regions of the template were further subdivided into a set of smaller compact regions, yielding a finer partition of the cerebral cortex into 424 and 789 regions (about 6 and 3 cm^2 each respectively). These finer partitions were then registered on the individual brains following the Freesurfer dedicated procedure. Finally, these regional partitions were registered using linear transformations previously calculated to the DWI and rsfMRI data of the subjects in order to derive corresponding matrices of SC and FC respectively.

Anatomical wiring

To quantify SC, we used the probabilistic white matter fiber tracking method (Behrens et al., 2007) implemented in FSL to track all possible connections between all pairs of regions. For every voxel of the white matter we initiated 500 fiber samples. Starting points were chosen randomly within the voxel space. Initial fiber orientation was randomly chosen and then fiber grew in the two opposite directions with a propagation step set at 0.5 mm and a maximal fiber curvature at 80° (no anisotropy constraint). Fiber tracking was stopped when samples reached the cortical surface. An index of structural connectivity between two regions was then defined as the proportion of fiber samples connecting these two regions per unit surface. This index was further divided by the average fiber length to account for the bias of the method towards longer fibers. This structural connectivity index allowed us to build a structural connectivity matrix $\boldsymbol{D} = (D_{ij})$ for each subject, D_{ij} being the structural connectivity index from region i to region j, with no self-connections (i.e. $D_{ii} = 0$). $\boldsymbol{D}$ was then thresholded at 0.001; supra-threshold values were conserved as such. Likewise, we built a matrix $\boldsymbol{L} = (L_{ij})$ for each subject, with entry L_{ij} corresponding to the average fiber length between regions i and j.

BOLD signal

The time series of all voxels within a given region were spatially averaged to form the representative BOLD signal of that region. To remove spurious sources of variance, linear and quadratic drifts, motion parameters, averaged ventricular, white matter and global brain signals were regressed out, and finally time series were low-pass filtered (<0.1 Hz) (Fox et al., 2009; Van Dijk et al., 2010).

Summary

For each subject and spatial scale (160, 461 and 825 regions), the preprocessing yielded three matrices: one of SC, one of average fibers' length (necessary for models explicitly taking into account delays of conduction), and one matrix of FC. These matrices were also averaged across subjects to yield 'average subject' data.

Simulations

Models

We used seven generative models possessing various levels of complexity: the SAR model, a purely spatial model with no dynamics that expresses BOLD fluctuations within one region as a linear combination of the fluctuations in other regions; the Wilson–Cowan system, a popular model integrating excitatory and inhibitory neuronal populations; a rate model, which is a simplified version of the Wilson–Cowan system obtained by considering exclusively the excitatory population; the Kuramoto model, which simulates coupled oscillators; the Fitzhugh–Nagumo model, a reduction of the Hodgkin and Huxley model aiming at reproducing complex behaviors with explicit conductance-based dynamics; the neural-mass model, also based on models of conductances and featuring strong biophysiological constraints; and finally, the model of spiking neurons, the most constrained model in the current study, which models neuron populations as attractors. Model complexity was quantified by the amount of parameters present in each model. For most models, all parameters were taken from the original papers, except the global coupling strength which was optimized separately for each model (see below). For more details on the models, see Appendix A.

From SC to BOLD via simulated neuronal activity

All models took a SC matrix as input, and all but the SAR model were explicit models of neuronal activity over time. Simulated fMRI BOLD signals were obtained from simulated neuronal activity by means of the Balloon–Windkessel hemodynamic model (Larter and Brent, 1999; Friston, 2003). Global mean signal was then regressed out from each region's time series. Finally, simulated FC was computed as the pairwise
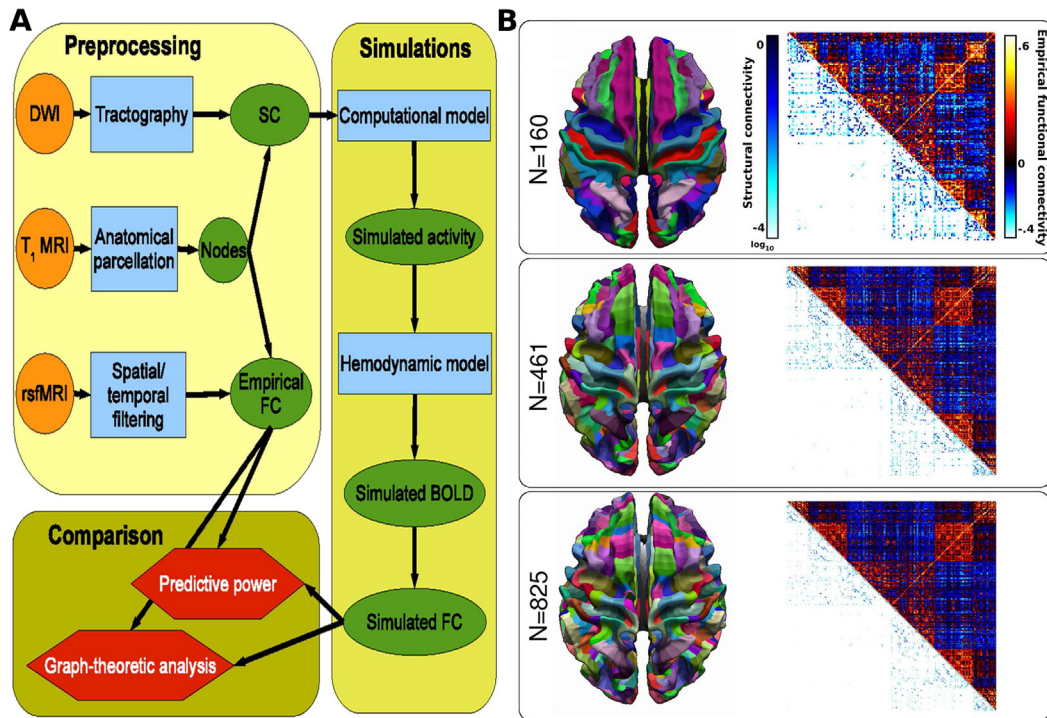
Fig. 1. Flowchart illustrating the processing pipeline and empirical data. (A) From the raw MRI data to the comparison of simulated functional connectivities. (Orange) raw data, (green) generated data, (blue) processes, and (red) comparative measures. (B) Brain parcellations and corresponding averaged structural (lower triangular part) and empirical functional (upper triangular part) connectivities for increasing spatial scales (from top to bottom).

Pearson correlation between simulated time series. For the SAR model, simulated FC could be directly derived from the analytical expression of the covariance matrix, see Eq. (A.2).

Numerical details of simulations

All simulations were performed in Matlab (The MathWorks Inc., Natick, MA), except for the spike model that had been implemented in the C language. The SAR model provides a closed form for the covariance matrix [see Eq. (A.2)] that can be used to directly compute the predicted functional connectivity. Dynamical models were simulated at a sampling frequency of 10 kHz. Simulations of the rate, Wilson–Cowan, Kuramoto, and Fitzhugh–Nagumo models relied on the Euler integration scheme, while Matlab ordinary differential equation solver was used for the neural-mass model. The resulting data were then downsampled to a sampling frequency of 1 kHz. The data corresponding to the first 20 s of the simulations were discarded from the analysis to avoid initial transient dynamics, resulting in 8 min of simulated brain activity. Simulated fMRI BOLD signal was obtained from neuronal activity by means of the Balloon–Windkessel hemodynamic model with a final sampling frequency of 2 Hz (Friston, 2003). The computational burden of the simulations according to the different models is summarized in Table 2.

After optimization (see below), in order to improve stability, we generated three runs of 8 min of BOLD activity with random initial conditions and averaged the corresponding run-related simulated FCs in order to obtain the simulated FC for each dynamical model and each subject.

Parameter optimization

All models took a normalized form of the SC matrix as an input, as well as the value of a global coupling strength parameter over all pairs of regions. We performed a model-specific optimization step over this latter parameter. For each model independently, we generated data with different matrix normalization strategies and values for the coupling parameter and saved the configuration that maximized predictive

power. For normalization of SC, we considered 2 approaches: spectral and row normalizations (Barnett et al., 2009). Spectral normalization consists in dividing the SC matrix by its spectral radius, i.e. the largest absolute value of its eigenvalues. Row normalization imposes that the matrix rows sum to 1 (Tononi et al., 1994). For the coupling parameter, we used known bounds whenever it was documented (for the SAR and Rate models) and had a purely exploratory approach otherwise. Optimization was performed separately for each model on the average subject at the lowest spatial scale to limit computational burden (see supplementary Fig. S1). For all the remaining parameters, specific for each model, values were taken mostly from the original papers (see Table 1).

Statistical analyses

For each of the 21 subjects and the 3 spatial scales (160, 461, and 825 regions), we obtained one matrix of empirical FC from Real data section and, from Simulations section, eight matrices of simulated FC, one for each computational model (including the one derived from SC). All matrices were vectorized to yield a total of 21 (subjects) × 9 (7 computational models + empirical FC + SC) = 189 vectors of dimension *#regions*(*#regions*−1)/2, representing the FC patterns. For a given subject, model and spatial scale, performance was assessed using predictive power, which was quantified by means of Pearson correlation between the pattern of empirical FC and that of FC simulated according to the model specified.

A 3-way ANOVA was performed on predictive power as a function of spatial scale (3 levels), computational model (8 levels) as a repeated measure over the 21 subjects, and including interactions. Box coefficient was applied for repeated measures and post-ANOVA analysis was performed using Tukey–Kramer HSD method (Tukey, 1953; Kramer, 1956). The validity of the assumptions was checked. The analysis was performed with JMP V10 software[4] (SAS Institute, Cary, NC) and STATA[5] (StataCorp, College Station, TX).

---

[4] http://www.jmp.com.
[5] http://www.stata.com.

Table 1
Computational models. Summary of models used.

Model	Variables	# of parameters	Parameters		References
SAR	y, BOLD signal	2	σ	Noise level	Tononi et al. (1994)
					Messé et al. (2014, 2015)
Rate	u, firing rate	4	v	Velocity	Galán (2008)
			τ	Time scale	Cabral et al. (2012)
			σ	Noise level	
Kuramoto	θ, oscillator phase	4	v	Velocity	Yeung and Strogatz (1999)
			ω	Intrinsic pulsation	Cabral et al. (2011)
			σ	Noise level	
Fitzhugh-Nagumo	x, slow state	8	v	Velocity	Stefanescu and Jirsa (2008)
	y, fast state		τ	Time scale ($\times 2$)	Ghosh et al. (2008)
			α, β, γ	Parameters	
			σ	Noise level	
Wilson-Cowan	E, excitatory neurons	10	v	Velocity	Wilson and Cowan (1972)
	I, inhibitory neurons		τ	Time scale ($\times 2$)	Deco et al. (2009)
			ω_I, ω_+	Synaptic strengths	
			a, b, c	Transfer function parameters	
			σ	Noise level	
Neural-mass	V, excitatory neurons	23	g_{ion}	Conductance ($\times 3$)	Breakspear et al. (2003)
	Z, inhibitory neurons		T_{ion}, δ_{ion}	Open ion channels parameters ($\times 3$)	Honey et al. (2009)
			ϕ, τ	Open potassium channels parameters	
			V, δ	Neural-mass parameters ($\times 2$)	
			V_{ion}	Nernst potential ($\times 3$)	
			a_{ii}, a_{ee}, a_{ie}	Synaptic strengths	
			r_{NMDA}	Number of NMDA receptors	
Spike attractor	E, excitatory neurons	35	N	Number of neurons ($\times 2$)	Deco and Jirsa (2012)
	I, inhibitory neurons		g_m	Conductance ($\times 2$)	
			C_m	Capacitance ($\times 2$)	
			V_L	Resting potential ($\times 2$)	
			V_{thr}	Subthreshold dynamics ($\times 2$)	
			V_{reset}	Membrane potential ($\times 2$)	
			τ_m	Time constant ($\times 2$)	
			V_I, V_E	Reserval potentials	
			τ_{rf}	Refractory period	
			$\omega_j, \omega_+, \omega$	Synaptic strengths	
			$g_{AMPA, ext}$	External synaptic conductances ($\times 2$)	
			$g_{AMPA,rec}$ g_{NMDA}, g_{GABA}	Recurrent synaptic conductances ($\times 2$)	
			$\tau_{NMDA}, \tau_{NMDA,rise}, \tau_{GABA}$	Rise and decay times	
			$\tau_{NMDA,decay}$	Decay time	
			α, β, γ	Parameters	

Graph-theoretic comparison

The generative models considered here have intrinsic differences, expressed in the diversity of their generative equations. Because of this complexity, it is difficult to analyze and understand the role that these theoretical differences play in the relative differences in performance. One way of further characterizing the relationships between models is to study how the 189 FC patterns (corresponding to different subjects and different origins: empirical FC or predictor from SC, SAR, and computational models) are related with one another from a graph-theoretic standpoint. In this perspective, a graph is defined where each of the 189 FC patterns is a node and the similarity between any two nodes is quantified using partial correlation (see below). Using tools from graph theory, we can characterize the main paths connecting simulated to empirical FCs. We can quantify whether there is a shortest path of a given model to empirical data through another model. We can further quantify whether models tend to have shortest paths all going through the same 'central' model in order to reach empirical data.

We computed the correlation between all pairs of the 189 FC patterns at a given scale. The resulting 189-by-189 correlation matrix was then transformed into a matrix of partial correlation, in order to remove confounding effects of indirect similarity and only keep effects that are more closely related to direct relationships (Whittaker, 1990; Fitch and Jones, 2009). Such an approach has been used in various contexts to explore the organization of brain networks, using fMRI-based FC analyses (Marrelec et al., 2006; Nakamura et al., 2009) and measures of cortical

Table 2
Computational burden. Mean (standard deviation) time across subjects, for each spatial scale and computational model.

Model	Spatial scale					
	160 regions		461 regions		825 regions	
SAR	14 ms	(1 ms)	83 ms	(2 ms)	134 ms	(7 ms)
Rate	1 h 31 min	(7 min)	10 h 27 min	(36 min)	1 day 12 h	(3 h)
Kuramoto	1 h 41 min	(9 min)	11 h 1 min	(47 min)	2 day 13 h	(3 h)
Fitzhugh–Nagumo	1 h 22 min	(3 min)	9 h 53 min	(21 min)	2 day 8 h	(4 h)
Wilson	1 h 21 min	(3 min)	9 h 58 min	(23 min)	1 day 22 h	(10 h)
Neural mass	3 h 35 min	(3 min)	7 h 49 min	(4 min)	14 h 5 min	(7 min)
Spike	1 day 1 h	(15 min)	3 day 11 h	(2 h)	7 day 3 h	(3 h)

thickness (Bassett et al., 2008). The resulting 189-by-189 partial correlation matrix was then used to define a weighted graph, the weight between two FC patterns being defined as the absolute partial correlation between these two patterns. From this graph, we computed graph-theoretic measures of centrality, such as degree (weighted), efficiency and betweenness centrality (Rubinov and Sporns, 2010). For graph measures based on distance (betweenness centrality and efficiency), weights were converted into lengths or distances by the inverse transform.

In order to investigate more specifically the within-subject features of the different patterns, we also performed the same kind of analyses but at the individual level. For each of the 21 subjects, we computed the correlation between the 9 (7 computational models + SC + empirical FC) corresponding FC patterns, leading to a 9-by-9 correlation matrix that we transformed into a partial correlation matrix. From the absolute values of partial correlations, we computed the same measures of centrality as above. Additionally, we computed the shortest paths from SC and simulated FCs to empirical FC using Dijkstra's algorithm from distance values (Dijkstra, 1959), for a total of 8 shortest paths per subject. For each model, we then computed the fraction of these 8 shortest paths that contained the model. This measure corresponds to the measure of betweenness centrality constrained to paths leading to empirical FC. With this measure, we aimed at identifying possible models through which most other models' shortest paths go through before reaching empirical data.

All analyses were implemented using Matlab (The MathWorks Inc., Natick, MA). We used metrics designed for weighted graphs from the Brain Connectivity Toolbox[6] (Rubinov and Sporns, 2010). Classical statistical inference was used to test differences at $p < 0.05$ significance. Correction for multiple comparisons, when required, was performed using the Bonferroni Holm method Holm (1979).

Results

Predicting empirical FC

The predictive power of models as a function of scale and their specific contribution are represented in Fig. 2. Significant effects (p-values estimated at a 10^{-6} max precision) were observed for the three main factors (3-way ANOVA: scale, $F = 683$, $p < 10^{-6}$; model, $F = 358$, $p < 10^{-6}$; subject, $F = 14$, $p < 10^{-6}$) as well as for the model * scale interaction ($F = 40$, $p < 10^{-6}$). Interactions subject * scale ($F = 1.9$, $p = 0.002$) and subject * model ($F = 1.5$, $p = 0.002$) were also significant. However, because of the large number of observations, the statistical power of the tests used was high, mechanically increasing the degree of statistical significance. By contrast, the mean-square values associated with between-scale and between-model variability were found to be much larger than those associated with between-subject variability and variability induced by interaction of scale and model with subject. Thus we decided to ignore the factor 'subject' in further analyses. The post-ANOVA analysis separated four groups of models, from best to worst prediction:

- SAR;
- Rate, Wilson, Neural mass;
- Kuramoto, SC, Spike; and
- Fitzhugh–Nagumo.

The SAR model performed better than other models in most cases, except for the Kuramoto model in two subjects with 160 regions, and for the Wilson model in three subjects with 461 regions and two subjects with 825 regions.

Analysis of partial correlation matrices

Results pertaining to partial correlation are summarized in Fig. 3. The first observation was a clear separation between empirical and simulated FC patterns. This was confirmed by spectral clustering of the partial correlation matrix, where a two-class clustering led to a partition of the FCs in a group containing all empirical FCs and the other group containing all simulated FCs.

The average within-model partial correlation was significantly larger than the average between-model and between-subject partial correlation ($p < 10^{-6}$). Therefore, the FC patterns differed more between models than within a model across subjects. Partial correlations between the SAR and the other models were higher within- than between-subject ($p < 10^{-6}$). Partial correlations between SCs and simulated FCs were generally negative and significantly lower within subject than between models and between subjects ($p < 10^{-6}$), except for SAR model for which simulated FCs were significantly higher ($p < 10^{-6}$). Finally, partial correlation values within subject and between all models but SC and the SAR were only slightly or not significantly different from partial correlation values between models and between subjects ($p = 0.0007$, $p = 0.009$ and $p = 0.06$, for scales of 160, 461 and 825 regions, respectively). In other words, these other models did not appear to be clearly correlated with one another even within the same subject. In summary, all FCs generated with the same model but for different subjects were correlated, while, for a given subject, all models seemed to be correlated with the SAR model and SC but not correlated with one another. This suggests that, at least within subject, the SAR model and/or SC might be more 'central' from a graph-theoretic standpoint.

Graph-theoretic comparison

Group analysis

The results of the graph theory analysis for the whole group of subjects are summarized in Fig. 3. All three measures of centrality (degree, efficiency and betweenness centrality) were significantly higher for FC patterns derived from the SAR than from other models (all $p < 0.05$, paired-tests corrected for multiple comparisons), at the exception of the measure of betweenness centrality at the lowest spatial scale, for which SC and the SAR did not significantly differ. The centrality of empirical FC patterns was often significantly below (53% of the tests) that of simulated FCs.

Individual analyses

Overall, at the individual level, the results remained consistent with the group analysis (see Fig. 4). The SAR was always ranked as the most 'central' model, or hub, for all three measures of centrality, for all subjects and scales, with centrality measures that were always significantly higher than those of other models (all $p < 0.05$, paired-tests corrected).

The SAR model also appeared to be in a pivotal position in the individual graphs. Its simulated FCs were topologically closest, in terms of shortest path, to empirical FCs (90% of tests significant). It is also this model through which most shortest paths go to reach empirical FC (80%, 86% and 82% for scales of 160, 461 and 825 regions, respectively).

Discussion

In the present study, we performed an extensive comparison of seven mainstream computational models of brain activity that were used to relate structural and functional connectivity derived from MRI. The simulations were performed using models of various levels of complexity on a dataset of 21 subjects at 3 spatial scales. We investigated the behavior of the simulated FC patterns when compared to empirical FC patterns but also in comparison to one another. We observed that (i) there were significant effects of scale and model on predictive power; (ii) among all models, the simplest model, the SAR model, was
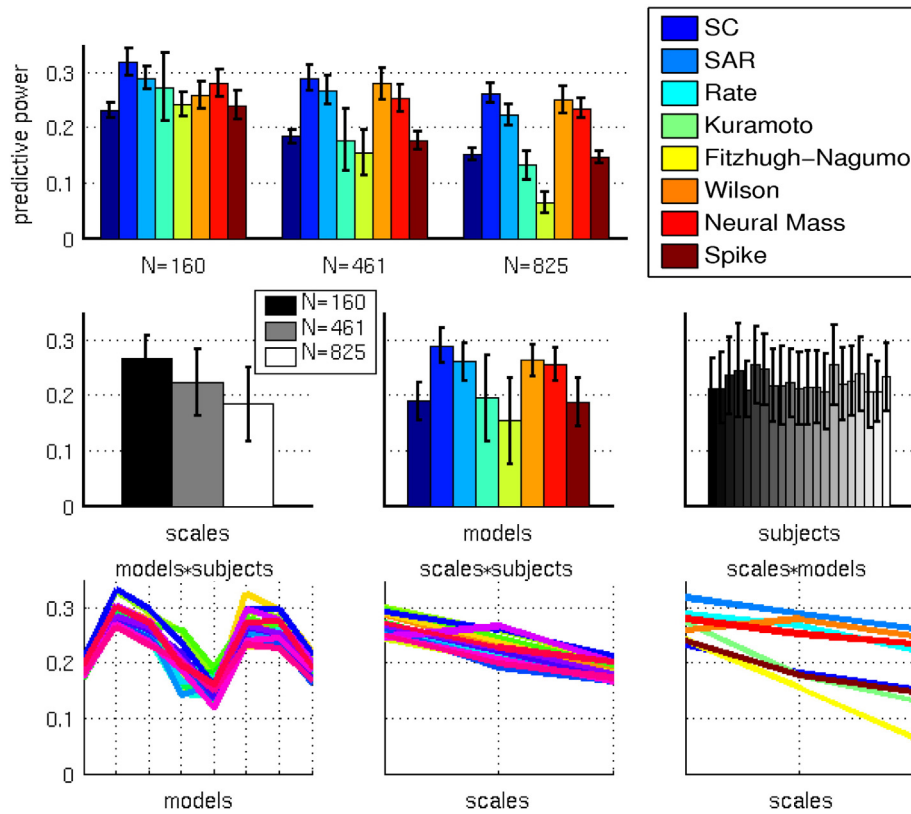
Fig. 2. Predictive power. Top: Predictive power as a function of model and spatial scale across subjects (means and standard deviations). Middle: Specific contribution of factors 'scale', 'model' and 'subject'. Bottom: Interactions between factors.

found to consistently perform better than the other models; (iii) this model also appeared more 'central' from a graph theory perspective; and (iv) by contrast, empirical FC only appeared weakly correlated with simulated FCs, and appeared as 'peripheral' in the graph analysis.

A variety of models

In recent years, there has been a growing interest in the use of computational models of brain activity to relate structural and functional connectivity from MRI in a generative manner. Various alternative models have been proposed to perform such analyses. In the present study, we considered 6 generative models, plus a simple linear model (SAR) and prediction from SC alone. The generative models considered ranged from a simplification of a Wilson–Cowan model (Rate) to a complex model of neuronal dynamics (Spike). The models considered are quite different in their origins, definitions, complexities, and parameters (see Appendix A). For instance, their complexity ranged from 2 parameters and an average computation time of 14 ms per subject (for 160 regions; the SAR) to 35 parameters and an average computation time of 1 day and 1 h per subject (Spike). These models displayed oscillatory behaviors and dynamics that can be quite different (Fig. 5). Unsurprisingly, this variety of behaviors resulted in a variety of simulated FC patterns. As shown by our graph-theoretic analysis, these patterns seemed to share some commonalities, in particular for simulations coming from the same generative model or for the same subject (and only specific models). Our results showed that simulated FCs tended to cluster by model rather than by subject. In other

words, the differences observed in simulated FC patterns were more a reflection of the differences between models than a reflection of the between-subject variability induced by differences in structural connectivity. We interpret this as evidence that the models used here are able to simulate a variety of FC patterns, with differences that are non-trivial and complex.

Predictive powers

This variety of FC patterns had an effect on the predictive power, as supported by our ANOVA, which found an effect of scale, model, as well as of model ∗ scale interaction. Scale had a negative effect on the predictive power. Regarding the global effect of the model, while we expected more complex models to have better predictive power, we observed a reverse trend, in that predictive power was found to be negatively correlated with both the number of parameters (but the effect was not significant) and the computation time (significant). When considering the model ∗ scale interaction, we observed behaviors (see Fig. 2, bottom right) which, albeit similar, are quite hard to interpret in their differences. The factor subject had little influence (see Fig. 2, middle right, bottom left and center) on the predictive power. Overall, despite these effects, the predictive values that were reached remained in a limited range (0.2–0.3, for 160 regions) with a rather small upper bound. From these results, we conclude that all the models mostly differ in aspects that have relatively limited impact on their predictive power for FC over the range of parameters explored.

Fig. 3. Graph theoretic comparison of FC patterns: global analysis. (A) 12,720 × 189 matrix of FC patterns corresponding to the lowest spatial scale (160 regions). (B) Matrices of partial correlation between FC patterns (from low to high spatial scale, left to right). (C) Associated backbone layouts using a force-directed algorithm (Kamada and Kawai, 1989) for partial correlation matrices thresholded at a sparse density of 2%. (D) Graph-theoretical characteristics (degree, efficiency and betweenness centrality). Black codes for empirical FC.
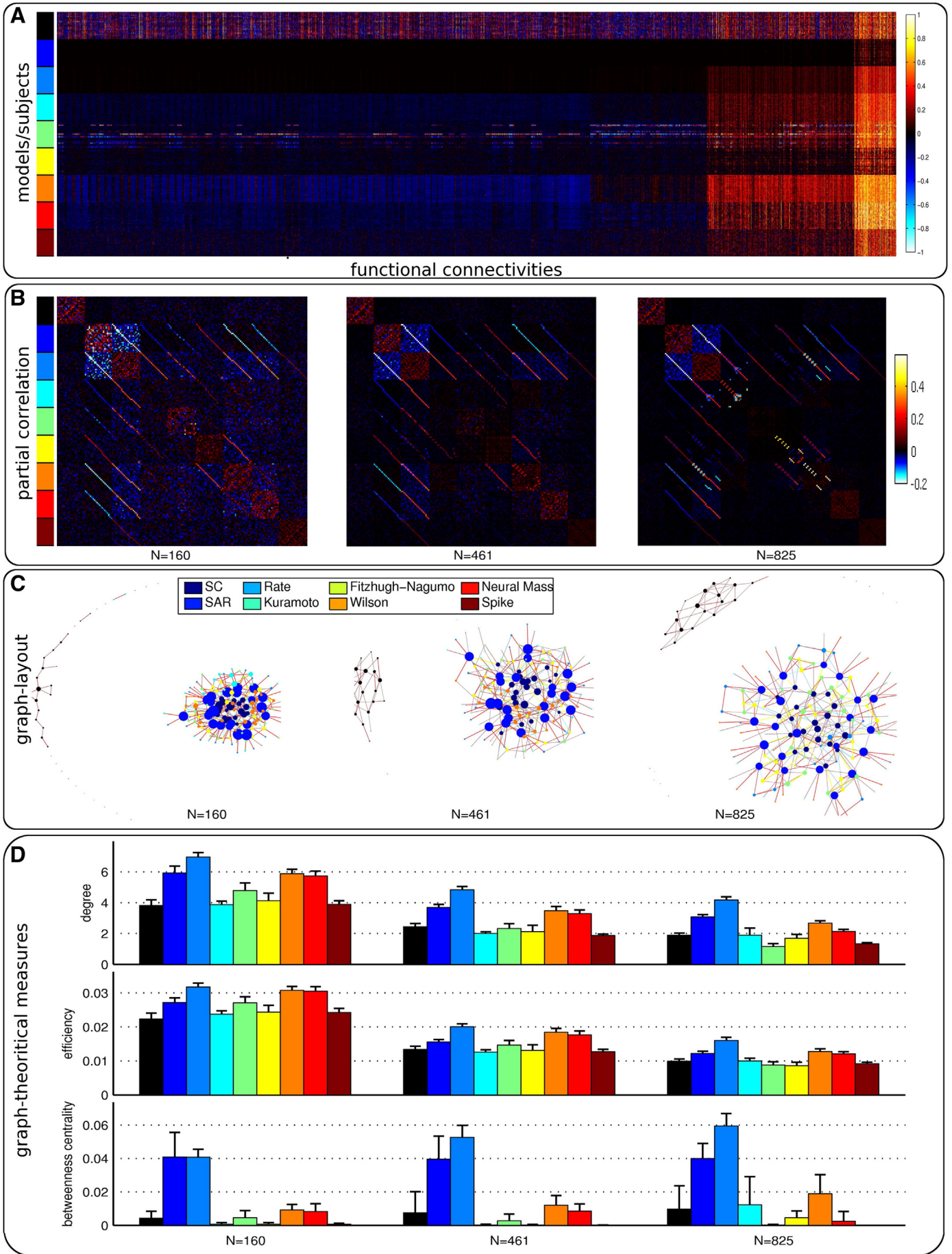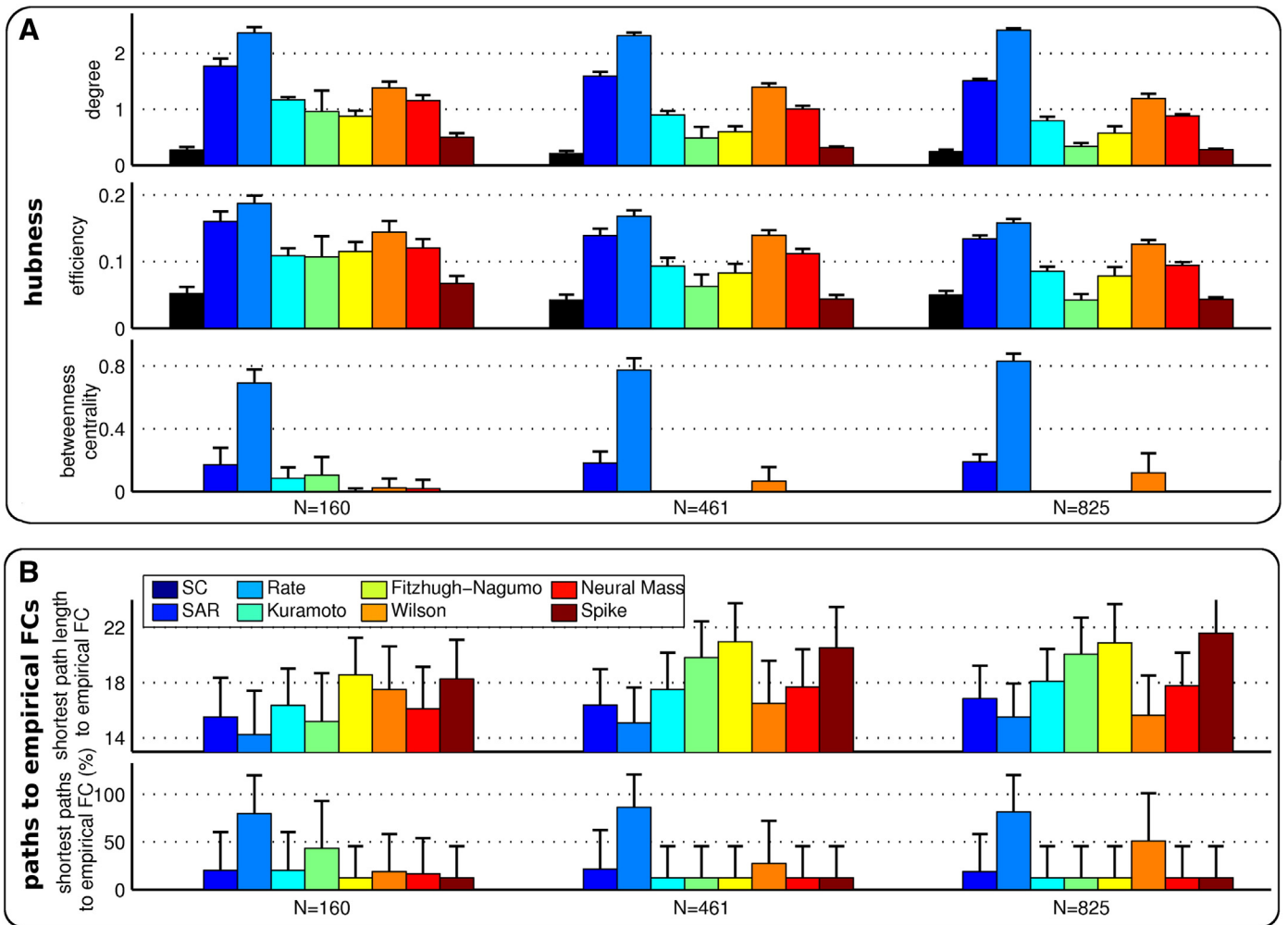
Fig. 4. Graph-theoretic comparison of FC patterns: individual analyses. Characteristics across subjects and spatial scales. From top to bottom: degree, efficiency, betweenness centrality, shortest path length to empirical FC, and proportion of shortest paths to empirical FCs passing through a given model. Color code models as in Fig. 2 and black color codes for empirical FC.

The core model of SAR

In our graph-theoretic analysis, the SAR model was characterized by a large within model similarity, as well as a relatively large similarity with FC generated by other models for the same subject. This is to be contrasted with other models, which mostly exhibited similar patterns within model. Quantitatively, this translated into large values of centrality, such as degree, efficiency and betweenness centrality. The centrality of the SAR in the graph suggests that models' predictive power is related to properties that are emphasized in the SAR. Since the SAR is essentially a linear process, its centrality suggests that the predictive power of other models is mainly explained by their linear component.

Structural connectivity estimation

Of course, data quality has a key influence on the performance of the models with respect to empirical FC. In particular, current measures of DWI-based tractography have well-known limitations. For instance, it is known that tractography tends to under-estimate the presence of interhemispheric fibers, notably between homologous regions. We previously reported on this issue with the same data and it was shown that manipulating interhemispheric connectivity had a strong influence on predictive power (Messé et al., 2014). Based on this previous experience, though, we expect an increase in SC estimation to mostly lead to an increase in the global level

of predictive power without modifying the behavior of models relative to one another.

Beyond FC: the heuristic value of computational models

The validation of computational models in predicting brain spontaneous activity, or resting-state, strongly depends on the features of the signal that we are interested in. Here, we focused on how models can be used to relate structural connectivity and functional connectivity in MRI. In this particular case, which is of high interest in multimodal MRI, a classical approach is to compare the simulated and empirical patterns of FC, e.g., using correlation (Honey et al., 2009). Such an approach should be considered as the first step of a complete investigation of the heuristic value of simulation models (Cabral et al., 2014), including their capacity to reproduce the dynamical properties of FC (Chang and Glover, 2010; Handwerker et al., 2012; Smith et al., 2012; Hutchison et al., 2013; Allen et al., 2014), to identify resting state networks (Beckmann and Smith, 2005; Damoiseaux et al., 2006), or even to reproduce properties observed at finer temporal scales with electro- and magnetoencephalography (Mantini et al., 2007; Brookes et al., 2011; Hipp et al., 2012), see, e.g. Messé et al. (2014) about the first two aspects.

Conclusion

We conclude that the computational models we compared, which display oscillatory behaviors and dynamics that can be quite different,
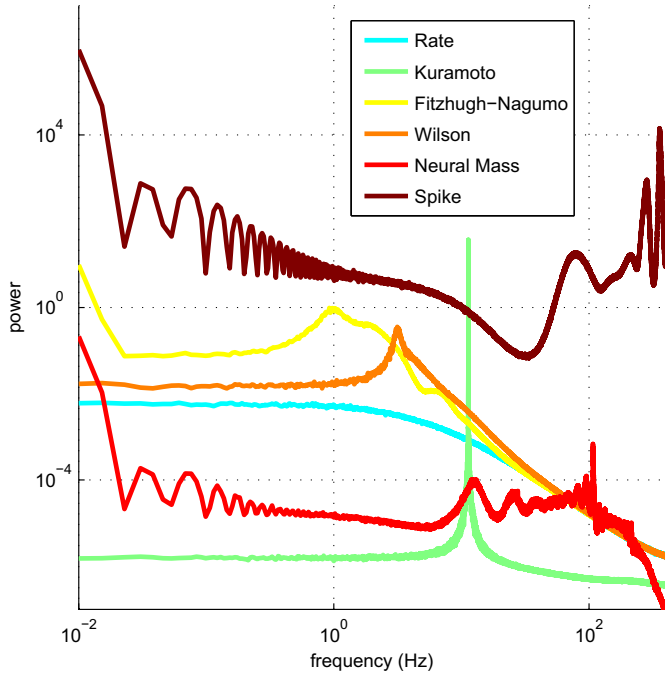
Fig. 5. Power spectrum. Averaged power spectrums across regions and runs of the neuronal activity, from one typical subject and for the different computational models (Fast Fourier Transform was used along with the Welch method). Color code models as in Fig. 2.

nevertheless mostly differ in aspects that have little impact on their overall predictive power for FC, over the range of parameters explored. As reflected in our graph analysis, beyond their basic differences, their ability to predict FC from SC appears to mostly reduce to a simple core (stationary) linear process that is explicitly embodied by the SAR model. This, along with the models' limited predictive power with respect to empirical FC, demonstrates the limited value of such modeling approaches in their current form for predicting observed functional connectivity.

Supplementary data to this article can be found online at http://dx.doi.org/10.1016/j.neuroimage.2015.02.001.

Acknowledgments

Appendix A. Description of generative models

The *SAR model* consists of expressing the BOLD signal $\mathbf{y} = (y_i)$ as a linear combination of the fluctuations within other regions (Tononi et al., 1994; Messé et al., 2014, 2015)

$$y_i = k\sum_{j\neq i} D_{ij}y_j + \sigma\nu_i. \tag{A.1}$$

In this notation, k is a parameter of spatial autoregression, σ is the noise level, and $\nu = (\nu_i)$ stands for uncorrelated white Gaussian noise with zero mean and unit variance. The relative values of k and σ quantify the balance between the part of signal that can be accounted for by the activity of other regions and the structural properties of the network ($\sum_{j\neq i} D_{ij}y_j$) and the part of the signal that can be interpreted as being endogenous to region i (ν_i). $\mathbf{y}$ is further assumed to be multivariate normal with zero mean and covariance matrix that can be calculated from Eq. (A.1) as

$$\sigma^2(\mathbf{I}-k\mathbf{D})^{-1}(\mathbf{I}-k\mathbf{D})^{-t}, \tag{A.2}$$

where $\mathbf{I}$ stands for the identity matrix and "^{t}" is the regular matrix transposition. In the simulations, σ was set to one. While noise level scales overall covariance level, it does not affect the resulting functional connectivity.

Wilson–Cowan model explores large ensembles of excitatory (E) and inhibitory (I) neurons using a mean-field approach (Wilson and Cowan, 1972; Deco et al., 2009). The dynamics is governed by the following equations:

$$\tau_E\frac{\partial E_i(t)}{\partial t} = -E_i(t) + \phi\left(I_b + k\sum_j D_{ij}E_j\left(t-\tau_{ij}\right) - I_i(t)\right) + \sigma\nu_i$$

$$\tau_I\frac{\partial I_i(t)}{\partial t} = -I_i(t) + \phi(\omega_I E_i(t)) + \sigma\nu_i,$$

with $D_{ii} = \omega_+/k$, and where τ_E and τ_I correspond to the time constant (or scale) of the excitatory and inhibitory population, respectively. ω_I is the action level of the excitatory population on the inhibitory population, ω_+ is the self-retroaction of excitatory population. I_b is a diffuse spontaneous background input. τ_{ij} is the propagation delay between regions i and j, based on the average fiber tract length between regions scaled by axonal velocity, v, i.e. $\tau_{ij} = L_{ij}/v$. ν is a random fluctuating input accounting for sources of biophysical variability and was defined as in the SAR model. The transfer function ϕ accounts for the saturation of firing rates in neuronal populations and is modeled by a sigmoid: $\phi(x) = \frac{c}{1-e^{-a(x-b)}}$. Parameters were set to (Messé et al., 2014): $\tau_I = \tau_E = 20$ ms; $\omega_I = 0.5$; $\omega_+ = 0.5$; $v = 10$ m/s; $I_b = 0$; $\sigma = 0.25$; $a = 5$; $b = 0$; and $c = 2$.

The *Rate fluctuations model* is a simplification of the Wilson–Cowan system (Galán, 2008; Cabral et al., 2012), where inhibitory populations and saturation function ϕ were removed.

$$\tau\frac{\partial u_i(t)}{\partial t} = -u_i(t) + k\sum_{j\neq i} D_{ij}u_j\left(t-\tau_{ij}\right) + \sigma\nu_i$$

Here: $\tau = 20$ ms; $v = 10$ m/s; and $\sigma = 0.25$ as in Cabral et al. (2012).

The *Kuramoto model* is composed of a set of coupled oscillators Yeung and Strogatz (1999), Cabral et al. (2011). The model equation reads:

$$\frac{\partial\phi_i(t)}{\partial t} = 2\pi f_i + k\sum_{j\neq i} D_{ij}sin\left(\phi_j\left(t-\tau_{ij}\right) - \phi_i(t)\right) + \sigma\nu_i,$$

where θ_i and f_i stand for the phase and intrinsic frequency of region i. Parameter values were taken from Cabral et al. (2011): $f_i = 60$ Hz; $v = 10$ m/s; and $\sigma = 1.25$ rd.

Fitzhugh–Nagumo model is composed of two nested variables Stefanescu and Jirsa (2008), Ghosh et al. (2008):

$$\tau_x\frac{\partial x_i(t)}{\partial t} = \gamma x_i(t) - \frac{x_i^3(t)}{3} - y_i(t) + k\sum_{j\neq i} D_{ij}x_j\left(t-\tau_{ij}\right) + \sigma\nu_i$$

$$\tau_y\frac{\partial y_i(t)}{\partial t} = -\beta y_i(t) + x_i(t) + \alpha + \sigma\nu_i,$$

where $\tau_x = 20$ ms; $\tau_y = 100$ ms; $v = 10$ m/s; $\sigma = 0.25$; $\alpha = 0.8$; $\beta = 0.6$; and $\gamma = 1$ as in Messé et al. (2014).

The *Neural-mass model* is a nonlinear biophysical model of neuronal dynamics relying on the Hodgkin–Huxley model (Breakspear et al., 2003; Honey et al., 2009). The main dynamical variables are the mean membrane potential of excitatory and inhibitory populations (V and Z, respectively), which are governed by the conductance of sodium, potassium and calcium ions, and the passive conductance of leaky ions, g_{ion}. The total current flow across pyramidal cell membranes is given by:

$$\frac{\partial V_i(t)}{\partial t} = -m_{\mathbf{Ca}}(g_{\mathbf{Ca}} + r_{\mathbf{NMDA}}a_{ee}k\sum_j D_{ij}Q_{V_j})(V_i(t) - V_{\mathbf{Ca}})$$
$$-(g_{\mathbf{Na}}m_{\mathbf{Na}} + a_{ee}k\sum_j D_{ij}Q_{V_j})(V_i(t) - V_{\mathbf{Na}})$$
$$-g_{\mathbf{K}}W(V_i(t) - V_{\mathbf{K}}) - g_{\mathbf{L}}(V_i(t) - V_{\mathbf{L}})$$
$$+a_{ie}ZQ_{Z_i} + a_{ne}I_\delta$$
$$\frac{\partial Z_i(t)}{\partial t} = b\Big(a_{ii}V_iQ_{V_i} + a_{ni}I_\delta\Big),$$

with $D_{ii} = (1-k)/k$, and where m_{ion} and V_{ion} are the fraction of open ion channels and the Nernst potential for that ion species, respectively. For large ion channel population, the fraction of open ion channels is given by the sigmoid-shaped neural activation function,

$$m_{ion} = \frac{1}{2}\left(1 + \tanh\left(\frac{V - T_{ion}}{\delta_{ion}}\right)\right),$$

except for the potassium channels that decay exponentially,

$$\frac{\partial W}{\partial t} = \frac{\phi(m_{\mathbf{K}} - W)}{\tau}.$$

Q_V and Q_Z represent the average firing-rates of excitatory and inhibitory neurons,

$$Q_X = \frac{Q_{X_{max}}}{2}\left(1 + \tanh\left(\frac{X - X_T}{\delta_X}\right)\right).$$

I_δ corresponds to nonspecific subcortical excitation. a_{xy} scales the x-to-y synaptic strength and $r_{\mathbf{NMDA}}$ corresponds to the number of NMDA receptors. Parameters are set to values taken from Honey et al. (2009).

The *Spiking neurons model* models each region as a biophysically realistic attractor consisting of mutually interconnected populations of excitatory pyramidal neurons and inhibitory neurons (Deco and Jirsa, 2012). This type of attractor network of spiking neurons is a dynamical system with an intrinsic tendency to settle in stationary states, also called attractors, typically characterized by a stable pattern of firing activity. Small perturbations may induce transitions between different stable attractors. Mean-field approximation yields a set of nonlinear equations of average firing rates of each population. For full details on the model definition and parameters, see Deco and Jirsa (2012).

References

Allen, E.A., Damaraju, E., Plis, S.M., Erhardt, E.B., Eichele, T., Calhoun, V.D., 2014. Tracking whole-brain connectivity dynamics in the resting state. Cereb. Cortex 24, 663–676.
Barnett, L., Buckley, C.L., Bullock, S., 2009. Neural complexity and structural connectivity. Phys. Rev. E 79, 051914.
Bassett, D.S., Bullmore, E., Verchinski, B.A., Mattay, V.S., Weinberger, D.R., Meyer-Lindenberg, A., 2008. Hierarchical organization of human cortical networks in health and schizophrenia. J. Neurosci. 28, 9239–9248.
Beckmann, C.F., Smith, S.M., 2005. Tensorial extensions of independent component analysis for multisubject FMRI analysis. NeuroImage 25, 294–311.
Behrens, T.E.J., Johansen-Berg, H., Jbabdi, S., Rushworth, M.F.S., Woolrich, M.W., 2007. Probabilistic diffusion tractography with multiple fibre orientations: what can we gain? NeuroImage 34, 144–155.
Breakspear, M., Terry, J.R., Friston, K.J., 2003. Modulation of excitatory synaptic coupling facilitates synchronization and complex dynamics in a biophysical model of neuronal dynamics. Netw. Comput. Neural Syst. 14, 703–732.
Breakspear, M., Jirsa, V., Deco, G., 2010. Computational models of the brain: from structure to function. NeuroImage 52, 727–730.

Brookes, M.J., Woolrich, M., Luckhoo, H., Price, D., Hale, J.R., Stephenson, M.C., Barnes, G.R., Smith, S.M., Morris, P.G., 2011. Investigating the electrophysiological basis of resting state networks using magnetoencephalography. Proc. Natl. Acad. Sci. U. S. A. 108, 16783–16788.
Cabral, J., Hugues, E., Sporns, O., Deco, G., 2011. Role of local network oscillations in resting-state functional connectivity. NeuroImage 57, 130–139.
Cabral, J., Hugues, E., Kringelbach, M.L., Deco, G., 2012. Modeling the outcome of structural disconnection on resting-state functional connectivity. NeuroImage 62, 1342–1353.
Cabral, J., Kringelbach, M.L., Deco, G., 2014. Exploring the network dynamics underlying brain activity at rest. Prog. Neurobiol. 114, 102–131.
Chang, C., Glover, G.H., 2010. Time-frequency dynamics of resting-state brain connectivity measured with fMRI. NeuroImage 50, 81–98.
Damoiseaux, J.S.S., Rombouts, S.A.R.B., Barkhof, F., Scheltens, P., Stam, C.J.J., Smith, S.M.M., Beckmann, C.F.F., 2006. Consistent resting-state networks across healthy subjects. Proc. Natl. Acad. Sci. U. S. A. 103, 13848–13853.
Deco, G., Jirsa, V.K., 2012. Ongoing cortical activity at rest: criticality, multistability, and ghost attractors. J. Neurosci. 32, 3366–3375.
Deco, G., Jirsa, V., Robinson, P.A., Breakspear, M., Friston, K., 2008. The dynamic brain: from spiking neurons to neural masses and cortical fields. PLoS Comput. Biol. 4, e1000092.
Deco, G., Jirsa, V., McIntosh, A.R., Sporns, O., Kotter, R., 2009. Key role of coupling, delay, and noise in resting brain fluctuations. Proc. Natl. Acad. Sci. U. S. A. 106, 10302–10307.
Dijkstra, E.W., 1959. A note on two problems in connexion with graphs. Numer. Math. 1, 269–271.
Fischl, B., Van der Kouwe, A., Destrieux, C., Halgren, E., Segonne, F., Salat, D.H., Busa, E., Seidman, L.J., Goldstein, J., Kennedy, D., Caviness, V., Makris, N., Rosen, B., Dale, A.M., 2004. Automatically parcellating the human cerebral cortex. Cereb. Cortex 14, 11–22.
Fitch, A.M., Jones, M.B., 2009. Shortest path analysis using partial correlations for classifying gene functions from gene expression data. Bioinformatics 25, 42–47.
Fox, M., Zhang, D., Snyder, A., Raichle, M., 2009. The global signal and observed anticorrelated resting state brain networks. J. Neurophysiol. 101, 3270–3283.
Friston, K.J., 2003. Dynamic causal modelling. NeuroImage 19, 1273–1302.
Galán, R., 2008. On how network architecture determines the dominant patterns of spontaneous neural activity. PLoS ONE 3, e2148.
Ghosh, A., Rho, Y., McIntosh, A.R., Kotter, R., Jirsa, V., 2008. Noise during rest enables the exploration of the brain's dynamic repertoire. PLoS Comput. Biol. 4, e1000196.
Hagmann, P., Cammoun, L., Gigandet, X., Meuli, R., Honey, C., Wedeen, V., Sporns, O., 2008. Mapping the structural core of human cerebral cortex. PLoS Biol. 6, e159.
Handwerker, D.A., Roopchansingh, V., Gonzalez-Castillo, J., Bandettini, P.A., 2012. Periodic changes in fMRI connectivity. NeuroImage 63, 1712–1719.
Hipp, J.F., Hawellek, D.J., Corbetta, M., Siegel, M., Engel, A.K., 2012. Large-scale cortical correlation structure of spontaneous oscillatory activity. Nat. Neurosci. 15, 884–890.
Holm, S., 1979. A simple sequentially rejective multiple test procedure. Scand. J. Stat. 6, 65–70.
Honey, C.J., Sporns, O., Cammoun, L., Gigandet, X., Thiran, J.-P., Meuli, R., Hagmann, P., 2009. Predicting human resting-state functional connectivity from structural connectivity. Proc. Natl. Acad. Sci. U. S. A. 106, 2035–2040.
Horwitz, B., 1990. Simulating functional interactions in the brain: a model for examining correlations between regional cerebral metabolic rates. Int. J. Biomed. Comput. 26, 149–170.
Hutchison, R.M., Womelsdorf, T., Gati, J.S., Everling, S., Menon, R.S., 2013. Resting-state networks show dynamic functional connectivity in awake humans and anesthetized macaques. Hum. Brain Mapp. 34, 2154–2177.
Kamada, T., Kawai, S., 1989. An algorithm for drawing general undirected graphs. Inf. Process. Lett. 31, 7–15.
Kramer, C.Y., 1956. Extensions of multiple range tests to group means with unequal numbers of replications. Biometrics 12, 307–310.
Larter, R., Brent, S., 1999. A coupled ordinary differential equation lattice model for the simulation of epileptic seizures. Chaos 9, 795–804.
Mantini, D., Perrucci, M.G., Del Gratta, C., Romani, G.L., Corbetta, M., 2007. Electrophysiological signatures of resting state networks in the human brain. Proc. Natl. Acad. Sci. U. S. A. 104, 13170–13175.
Marrelec, G., Krainik, A., Duffau, H., Pélégrini-Issac, M., Lehéricy, S., Doyon, J., Benali, H., 2006. Partial correlation for functional brain interactivity investigation in functional MRI. NeuroImage 32, 228–237.
Messé, A., Rudrauf, D., Benali, H., Marrelec, G., 2014. Relating structure and function in the human brain: relative contributions of anatomy, stationary dynamics, and non-stationarities. PLoS Comput. Biol. 10, e1003530.
Messé, A., Benali, H., Marrelec, G., 2015. Relating structural and functional connectivity in MRI: a simple model for a complex brain. IEEE Trans. Med. Imaging 34, 27–37.
Nakamura, T., Hillary, F., Biswal, B., 2009. Resting network plasticity following brain injury. PLoS ONE 4, e8220.
Rubinov, M., Sporns, O., 2010. Complex network measures of brain connectivity: uses and interpretations. NeuroImage 52, 1059–1069.
Smith, S.M., Jenkinson, M., Woolrich, M.W., Beckmann, C.F., Behrens, T.E.J., Johansen-Berg, H., Bannister, P.R., De Luca, M., Drobnjak, I., Flitney, D.E., Niazy, R.K., Saunders, J., Vickers, J., Zhang, Y., De Stefano, N., Brady, J.M., Matthews, P.M., 2004. Advances in functional and structural MR image analysis and implementation as FSL. NeuroImage 23, 208–219.
Smith, S.M., Miller, K.L., Moeller, S., Xu, J., Auerbach, E.J., Woolrich, M.W., Beckmann, C.F., Jenkinson, M., Andersson, J., Glasser, M.F., Van Essen, D.C., Feinberg, D.A., Yacoub, E.S., Ugurbil, K., 2012. Temporally-independent functional modes of spontaneous brain activity. Proc. Natl. Acad. Sci. U. S. A. 109, 3131–3136.
Stefanescu, R.A., Jirsa, V.K., 2008. A low dimensional description of globally coupled heterogeneous neural networks of excitatory and inhibitory neurons. PLoS Comput. Biol. 4, e1000219.

Tononi, G., Sporns, O., Edelman, G., 1994. A measure for brain complexity: relating functional segregation and integration in the nervous system. Proc. Natl. Acad. Sci. U. S. A. 91, 5033–5037.

Tukey, J. W., 1953. The problem of multiple comparisons, unpublished manuscript, Princeton Univ.

Van Dijk, K., Hedden, T., Venkataraman, A., Evans, K., Lazar, S., Buckner, R., 2010. Intrinsic functional connectivity as a tool for human connectomics: theory, properties, and optimization. J. Neurophysiol. 103, 297–321.

Whittaker, J., 1990. Graphical Models in Applied Multivariate Statistics. J. Wiley and Sons, Chichester.

Wilson, H.R., Cowan, J.D., 1972. Excitatory and inhibitory interactions in localised populations of model neurons. Biophys. J. 12, 1–24.

Woolrich, M.W., Stephan, K.E., 2013. Biophysical network models and the human connectome. NeuroImage 80, 330–338.

Yeung, M.K.S., Strogatz, S.H., 1999. Time delay in the Kuramoto model of coupled oscillators. Phys. Rev. Lett. 82, 648–651.